fluids

MDPI

Article

Dimensionless Analysis of Rough Roadway Airflow Distribution Based on Numerical Simulations

Zongcheng Jia [1], Qiang Zhao [1,*], Yan Zhao [1], Baoyu Cui [1] and Tao Song [2,3]

[1] School of Resources & Civil Engineering, Northeastern University, Shenyang 110819, China; 2410492@stu.neu.edu.cn (Z.J.); 2201139@stu.neu.edu.cn (Y.Z.); cuibaoyu@mail.neu.edu.cn (B.C.)
[2] State Key Laboratory of Intelligent Optimized Manufacturing in Mining& Metallurgy Process, Beijing 100160, China; songtao@bgrimm.com
[3] Beijing Key Laboratory of Process Automation in Mining & Metallurgy, Beijing 100160, China
* Correspondence: zhaoqiang@mail.neu.edu.cn

Abstract: As resources are extracted from the deeper sections of a mine, the ventilation network becomes increasingly complex. Consequently, determining the optimal installation location for speed-measuring equipment that accurately reflects the average wind speed along the roadway remains a challenging task. In this study, two three-dimensional geometric models, smooth and rough, were developed based on field conditions. The cross-sectional widths, heights, and flow velocities of the model channels were processed dimensionlessly. The dimensionless velocity distributions of the smooth and rough models were then analyzed for different Reynolds numbers. It was observed that the dimensionless average velocity ring distributions for the rough model were smaller than those for the smooth model. Additionally, the maximum values of dimensionless flow velocities were negatively correlated with the flow velocities under laminar flow conditions, whereas they largely overlapped under turbulent flow. The dimensionless distances of the average velocity rings from the top and sidewalls of the channel were studied and determined for both models across different flow regimes. Specifically, the dimensionless distance values $d\ (-)$ were found to be 0.111 for the smooth model and 0.101 for the rough model under the laminar regime. Under the turbulence regime, the corresponding values were 0.106 and 0.108. Likewise, the values of $h\ (-)$ were 0.135 and 0.135 for the smooth and rough models in the laminar flow regime, while under turbulent flow, the values were 0.131 and 0.162, respectively. The largest dimensionless velocity value was identified at the center of the velocity distribution circle. For corners that did not maintain simple parallelism with the walls, these regions were incorporated into the circle equation using the Least Squares Method, providing a theoretical basis for the placement of velocity-measuring equipment in practical applications. By using the sidewall as the reference coordinate, an appropriate mathematical model was employed to establish the functional relationship between the centerline velocity of the roadway and the dimensionless horizontal coordinate. The fitting results showed good agreement, and this model can be used to back-calculate and expand the potential installation locations for a mine anemometer.

Keywords: numerical simulation; mine tunnel; non-dimensionalization; characteristic distribution

check for updates

Academic Editor: D. Andrew S. Rees

Received: 11 February 2025
Revised: 6 March 2025
Accepted: 18 March 2025
Published: 23 March 2025

Citation: Jia, Z.; Zhao, Q.; Zhao, Y.; Cui, B.; Song, T. Dimensionless Analysis of Rough Roadway Airflow Distribution Based on Numerical Simulations. *Fluids* **2025**, *10*, 77. https://doi.org/10.3390/fluids10040077

Copyright: © 2025 by the authors. Licensee MDPI, Basel, Switzerland. This article is an open access article distributed under the terms and conditions of the Creative Commons Attribution (CC BY) license (https://creativecommons.org/licenses/by/4.0/).

1. Introduction

Mine ventilation is crucial for ensuring production safety and energy efficiency by supplying fresh air and removing contaminated air [1]. As mining operations extend

deeper underground, ventilation systems become increasingly complex, making precise measurement of the average air velocity in tunnels essential. The airflow in mine tunnels is highly irregular, influenced by factors such as tunnel shape, cross-sectional area, and support structures. These factors contribute to uneven velocity distribution, turbulence, and localized high-speed wind zones, complicating accurate airflow measurement. Statistical data indicate that ventilation failures have been a major cause of mine disasters, including gas and dust explosions [2]. Among ventilation parameters, air volume is the most critical and easily measurable, playing a key role in effective ventilation management. Accurate air volume measurements directly affect the performance of mine ventilation networks and system optimization efforts [3]. Therefore, developing a new method to determine the average velocity position with high accuracy is of significant practical importance.

Traditional ventilation network analysis software, such as Ventsim (URL: https://ventsim.com/), typically calculates only the average velocity, disregarding the non-uniform nature of the airflow. In the last century, researchers established a functional relationship between the average and maximum velocity in fully developed turbulent flow within pipes, supported by direct numerical simulations (DNSs) and experimental studies [4]. Currently, high-precision online monitoring systems are used to track airflow velocity and volume in tunnels. However, these systems usually measure velocity at a single point, which may not accurately represent the average velocity across the cross-section of tunnels. Several recent studies have explored airflow behavior in underground tunnels. In the main tunnel airflow distribution, numerical simulations have been used to develop characteristic equations describing average velocity distributions for rectangular, trapezoidal, and three-center arch cross-sections under both regular and irregular shapes [5–8]. Zhang et al. [9] combined theoretical analysis, numerical simulation, and field testing to determine the airflow velocity distribution in rectangular and semi-circular roadway sections. To improve the accuracy of airflow velocity measurements in coal mines, a COMSOL Multiphysics numerical (URL: https://www.comsol.com/) simulation analyzed the influence of inlet velocity distribution on tunnel sections. The results indicated that airflow velocity contours were generally parallel to the tunnel walls [10]. Although these investigations established the average velocity distribution and corresponding equations for typical tunnel sections, the models rely on regular geometries and lack dimensionless analysis of tunnel geometry and flow field data. Consequently, their applicability remains limited. In studies of airflow distribution in auxiliary ventilation ducts, Parra et al. [11] analyzed velocity and methane concentration distribution in ventilation systems operating in the cul-de-sac of a coal mine. Hasheminasab et al. [12] examined the ventilation performance of a working coal face section exposed to methane gas under the influence of auxiliary fans. Accurately measuring airflow velocity in underground environments remains challenging, due to the complexity of these conditions. Despite this, few studies have focused on improving velocity measurement techniques for mine ventilation systems. A recent study explored a novel method of determining the average velocity by tunnel particle image velocimetry (PIV) and numerical simulation using OpenFOAM, demonstrating that the single-point velocity is directly proportional to the average velocity [13]. Tominaga et al. [14] investigated rectangular cross-section flow under fully developed turbulence using a fiber-optic laser Doppler anemometer (FLDA). While these methods effectively measure tunnel velocity, they are not yet suitable for widespread engineering applications.

In summary, extensive research has been conducted globally on tunnel velocity distribution, leading to advancements in traditional ventilation velocity measurement. However, due to the unique characteristics of the mine environment and the specific requirements of engineering applications, applying these research findings in practical settings remains challenging. This study aims to analyze the dimensionless velocity distribution charac-

teristics of a three-center arched tunnel across different Reynolds number ranges, using a rough tunnel model. Additionally, it seeks to provide both theoretical and experimental foundations for optimizing the installation of velocity measurement equipment in underground environments.

2. Methodology

2.1. Physical Model

This paper constructs a geometric model based on the actual tunnel of Zijin Mining in Shanxi Province, as shown in Figure 1a. To enable laboratory examination, the original model was scaled down (42:1) and simplified, resulting in two versions: one with smooth walls and another with rough walls. The tunnel dimensions are 3000 mm in length, 120 mm in width, and 92.04 mm in height. The three-center arch section has an area of 10,104.78 mm^2, with a minor arch radius of 30 mm and a major arch radius of 90 mm. The geometric models are illustrated in Figure 1b,c. The smooth model is derived from the vertical stretching of the plane depicted in Figure 1b. To create a rough model that more accurately represents the actual roadway, concave and convex forms were excavated and infilled on the smooth model to maintain wall roughness within the range of 2–10 mm, thereby achieving similarity between the model and actual tunnel surface roughness, as shown in Figures 1d and 1e, respectively. Additionally, four other models were constructed through uniform scale expansion, with scaling factors of ×2, ×4, ×8, and ×10.

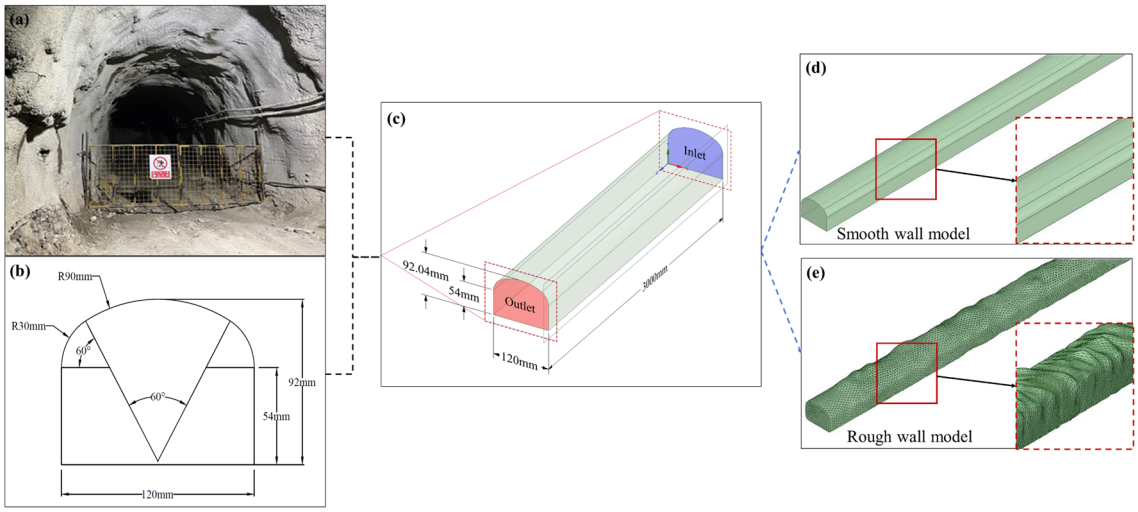


Figure 1. Ventilation tunnel laboratory model. (**a**) Actual tunnel model of Zijin Mining, located in Shanxi province; (**b**) physical model of three-center arch sections; (**c**) physical model of tunnel; (**d**) schematic of smooth model; and (**e**) schematic of rough model.

2.2. Mathematical Models

2.2.1. Governing Equations

The airflow in the tunnel is treated as an incompressible fluid, since its velocity is less than 0.3 times the speed of sound [15–17]. Moreover, the Reynolds number (*Re*) of the tunnel airflow exceeds 2100, indicating a turbulent flow regime [18–20]. Consequently, the numerical model for incompressible airflow in this study is developed based on the governing equations presented below.

The continuity equation is as follows:

$$\nabla \cdot \boldsymbol{v} = 0 \tag{1}$$

The momentum equation is as follows:

$$\frac{\partial}{\partial t}(\rho \boldsymbol{v}) + \nabla \cdot (\rho \boldsymbol{v}\boldsymbol{v}) = -\nabla p + \rho \boldsymbol{g} + \boldsymbol{F} \tag{2}$$

where ρ represents the air density, t is time, $\boldsymbol{v}$ is the air velocity, p is the static pressure, and $\rho \boldsymbol{g}$ and $\boldsymbol{F}$ are the gravitational and external body force.

2.2.2. Turbulence Models

Turbulence models in computational fluid dynamics (CFD) range in complexity from the basic zero-equation model to advanced methods, such as large-eddy simulation (LES) and detached-eddy simulation (DES). The Reynolds-averaged Navier–Stokes (RANS) approach serves as an intermediate model, and is widely applied in engineering due to its balance between computational efficiency and accuracy. Among these models, the k-epsilon and k-omega models are commonly employed in engineering evaluations [21–23]. This paper used the standard k-epsilon model as a reliable method for simulating airflow in the tunnel for mine ventilation assessment [24]. The turbulent kinetic energy, k, and its dissipation rate, ε, are governed by the subsequent equations:

The k equation is as follows:

$$\frac{\partial}{\partial t}(\rho k) + \frac{\partial}{\partial x_i}(\rho k u_i) = \frac{\partial}{\partial x_j}\left[\left(\mu + \frac{u_\tau}{\sigma_k}\right)\frac{\partial k}{\partial x_j}\right] + G_k + G_b + \rho\varepsilon - Y_m + S_k \tag{3}$$

The epsilon equation is as follows:

$$\frac{\partial}{\partial t}(\rho \varepsilon) + \frac{\partial}{\partial x_i}(\rho \varepsilon u_i) = \frac{\partial}{\partial x_j}\left[\left(\mu + \frac{u_\tau}{\sigma_\varepsilon}\right)\frac{\partial \varepsilon}{\partial x_j}\right] + C_{1\varepsilon}\frac{\varepsilon}{k}(G_k + G_b G_{3\varepsilon}) - C_{2\varepsilon}\rho\frac{\varepsilon^2}{k} + S_\varepsilon \tag{4}$$

where G_k and G_b denote the generation of turbulence kinetic energy due to the mean velocity gradients and buoyancy, respectively; Y_m denotes the contribution of the fluctuating dilatation; u_i represents the velocity component in the i-th direction; x_i denotes the spatial coordinate in the i-th direction; μ denotes the molecular viscosity of the fluid; σ_k represents the turbulent Prandtl number for k; σ_ε represents the turbulent Prandtl number for ε; and u_τ denotes the eddy viscosity. The values of $C_{1\varepsilon}$, $C_{2\varepsilon}$, $G_{3\varepsilon}$, and S_k are 1.44, 1.92, 0.09, and 1.0, respectively.

2.2.3. Entrance Region Length

In fluid dynamics, the entrance region length refers to the distance a flow travels after entering a conduit before reaching a fully developed state [25]. In turbulent flow, the characteristic length is generally defined by the following expression:

$$L_e = 1.359 D (Re_D)^{\frac{1}{4}} \tag{5}$$

In this study, Equation (5) is used to approximate the L_e of the three-center arch section tunnel, and all cross-sectional flow field analyses are carried out under the turbulence at the fully developed stage.

2.2.4. Least Squares Method for Solving Equation of Circle

The Least Squares Method (LSM) is a widely used optimization technique for data fitting and regression analysis [26,27]. Its primary objective is to minimize the sum of squared differences between observed data points and the predicted model, thereby providing an optimal representation of the underlying relationship. The LSM is computationally

efficient, particularly for linear regression, as it offers a closed-form analytical solution, eliminating the need for iterative methods such as gradient descent (GD), which require careful hyperparameter tuning. Additionally, the LSM is robust to minor data noise, as it minimizes the overall error, rather than focusing on individual discrepancies, making it less sensitive to outliers. Moreover, it seamlessly adapts to high-dimensional multivariate regression problems, while maintaining efficiency in large-scale data fitting. Under the assumption of Gaussian noise, the LSM provides the Best Linear Unbiased Estimator (BLUE), ensuring minimal variance among unbiased estimators. In this study, the coordinates of the circle's center are first established, followed by the calculation of the radius using the Least Squares approach. The procedure for determining the radius is outlined below, with the value of r derived from Equation (9).

$$(x-a)^2+(y-b)^2=r^2 \tag{6}$$

$$d_i^2=(x_i-a)^2+(y_i-b)^2 \tag{7}$$

$$f(r)=\sum_{i=1}^{n}\left(d_i^2-r^2\right) \tag{8}$$

$$\frac{df(r)}{dr}=0 \tag{9}$$

where x and y denote the horizontal and the vertical coordinates of any point on the circle, $(a,\ b)$ is the coordinate of the center of the circle, r represents the radius of the circle, x_i and y_i are the discrete points on the average velocity ring obtained from the simulation and d_i is calculated based on those, and $f(r)$ is the function of r.

2.2.5. Fitting Model

In this study, a model with a high goodness of fit was selected based on the obtained data using GraphPad Prism software (URL: https://www.graphpad.com/). The mathematical expression of the selected model is as follows:

$$V(-)=\frac{V_{max}w(-)}{K_m+w(-)} \tag{10}$$

where $w(-)$ is the dimensionless distance from the sidewalls, V is the velocity, $V(-)$ is the dimensionless velocity, and V_{max} and K_m are constants to be determined.

2.3. Dimensionless Treatment

Dimensionless treatment, also referred to as normalization, is a fundamental technique in scientific research and data analysis. The primary objective of this approach is to eliminate the influence of dimensional or variable fluctuations, thereby enabling the comparison and interpretation of data under a consistent standard, despite inherent dimensional differences [28].

In this study, dimensional analysis was employed to eliminate the influence of units on the results of numerical simulations by converting the tunnel length scale and flow velocity into dimensionless quantities. Specifically, the x and y coordinates were normalized by dividing them by 120 mm and 92.04 mm, respectively, as shown in Equations (11) and (12). A similar normalization approach was applied to the velocity field, as shown in Equation (13). Additionally, proportional scaling was applied to the enlarged model, where the dimensions and velocity were normalized in a similar manner, using their corresponding scaled values.

$$x\ (-)=\frac{x}{120} \tag{11}$$

$$y\,(-) = \frac{y}{92.04} \tag{12}$$

$$v\,(-) = \frac{v}{v_{in}} \tag{13}$$

where x is the horizontal coordinate and y is the vertical coordinate, both in mm; $x\,(-)$, $y\,(-)$ are the dimensionless coordinates of x, y, respectively; v is the real velocity of the flow pattern; v_{in} is the inlet velocity, which varies under different conditions; and $v\,(-)$ is the dimensionless velocity.

2.4. Simulation Condition

The physical model was discretized into control volumes using ICEM CFD and Fluent meshing, resulting in a mesh composed of approximately 950,000 elements. Mesh independence verification was performed by analyzing the dimensionless velocity along the tunnel's centerline, parallel to the x-axis, with the results shown in Figure 2. The element count is considered adequate for these simulations, as the flow field characteristics demonstrate minimal variation when the number of elements exceeds 166,000. This study aims to establish an optimal arrangement of hexahedral grids within the tunnel's center to accurately capture the airflow velocity distribution. To achieve this, the grid density is concentrated at the center, while the near-wall grids are relatively sparse. This issue is addressed by implementing an enhanced wall function, which ensures that the simulated results are both reliable and accurate. This approach guarantees a favorable value of y^+, thereby assuring the correctness and reliability of the simulation.

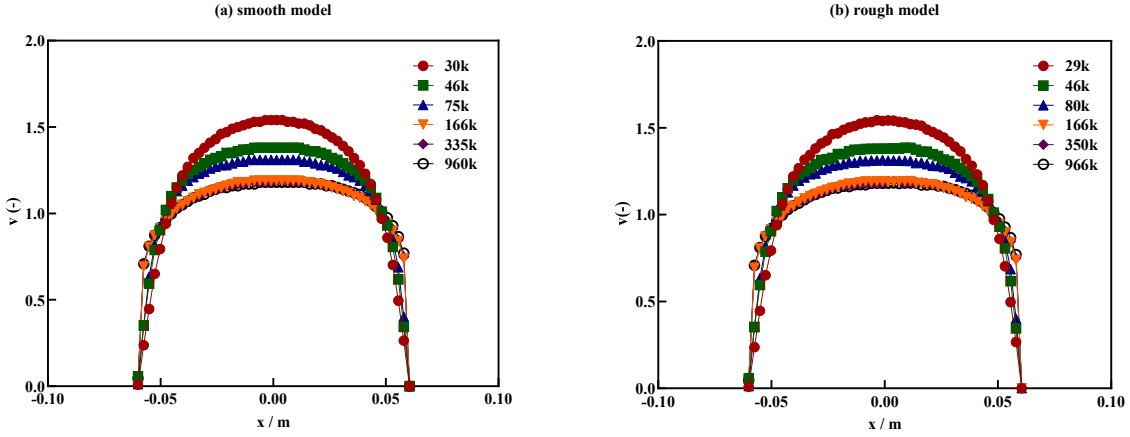


Figure 2. Results of mesh independence verification: (**a**) smooth model and (**b**) rough model.

The simulation work was conducted using a pressure-based solver, embedded in commercial ANSYS Fluent (v18.0) with Intel(R) Xeon(R) Platinum 8179 M processors (CPU 92 cores, 2.4 GHz, 128 G RAM) at Northeastern University, China. The segregated PISO algorithm was employed to solve the pressure–velocity field. The PRESTO! interpolation method was utilized for pressure solutions, and the Second-Order Upwind Scheme was applied for the transport equations of momentum and turbulence. The Least Squares Cell-based Method was used to compute gradient terms. To ensure numerical accuracy, the residual tolerance for all terms, including continuity, velocity, and epsilon, was maintained below 10^{-5}, with a fixed time step of 10^{-5} s.

The numerical simulation in this study is based on the following assumptions: (1) the air composition consists of a significant number of molecules, exhibiting uniformity and consistency both spatially and temporally; (2) no heat source is present at the boundaries of the fluid domain; and (3) under stable ventilation, underground dust becomes suspended, and its effects are neglected. The critical Reynolds number for the transition from laminar

to turbulent flow in the boundary layer flow on a flat plate is approximately 5×10^5 [29]. In contrast, for conventional duct flow, the flow is considered laminar at Reynolds numbers lower than 2100, and fully turbulent for Reynolds numbers greater than 4000 [30,31]. In this study, three velocity subgroups have been established to analyze the distribution of tunnel airflow in the turbulent case, accounting for the unique characteristics of a mine tunnel. The tunnel outlet is defined as the Pressure Outlet, with the relative pressure of 0 Pa. No slip condition was applied to the walls. More details about the boundary conditions of the three-center section tunnel are presented in Table 1. Furthermore, to ensure consistent scaling of the Reynolds number, the inlet velocity of the model is adjusted according to the corresponding scale, while the remaining boundary conditions are maintained as shown in Table 1.

Table 1. Operating conditions of three-center section tunnel.

Parameters	Value/Scheme	Comment
Inlet velocity/(m/s)	0.05, 0.10, 0.15, 0.20, 0.25, 0.30 5.0, 6.5, 8.0, 9.5, 11.0, 12.5, 15.0, 17.5, 20.0, 22.5, 25.0, 27.5	$1 < Re < 2100$ $2100 < Re < 10^5$ $10^5 < Re$
Outlet relative pressure/Pa	0	
Wall	No slip	
Wall function	Enhanced wall function	
Segregated algorithm	PISO	
Airflow iterations	2500	
Time step size	10^{-5}	
Gradient solver scheme	Least Squares Cell-based Method	
Momentum and turbulence solver scheme	Second-Order Upwind	
Pressure solver scheme	PRESTO!	

2.5. Model Validation

Model verification is an essential procedure before employing the proposed model for subsequent numerical experiments. Consistently with Ding's study [7,32], a model was developed to assess the accuracy and reliability of the proposed methodology, similar to the model introduced by Ding. Ding's experimental and simulation results show substantial agreement, utilizing key equipment such as the low-noise centrifugal blower (model DIF-2) with a maximum airflow capacity of 860 m^3/min and a rated power of 550 W, along with the LUGB/E type vortex flowmeter, which provides an accuracy of ±1.5% within a flow range of 133–1700 m^3/h. The detailed specifications of Ding's model are shown in Figure 3.

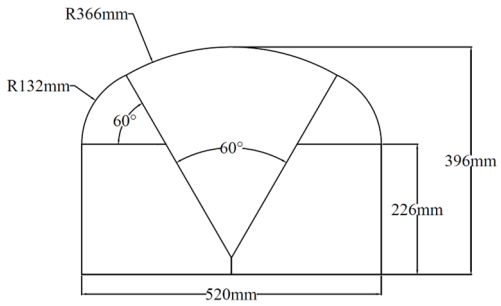


Figure 3. Physical model of Ding's experiments.

The standard k-epsilon model was utilized to simulate turbulent flow and diffusion, governed by numerous assumptions in the calculations. These assumptions include the incompressibility of air, the adiabatic nature of the tunnel walls, the absence of mass or

heat transfer across boundaries, the no-slip condition for the walls, the absence of obstacles such as personnel or vehicles, and the exclusion of dust effects. The model's boundaries are defined as follows: a Velocity Inlet boundary condition is applied at the roadway entrance, with a velocity of 5 m/s, and a Pressure Outlet boundary condition is specified at the pressure outlet, with a relative pressure of 0 Pa. Additional details about the model are provided in Table 2. Furthermore, all the flow field data were analyzed at locations where the turbulence had fully developed. The results of the model verification are presented in Figure 4.

Table 2. Geometric and operating conditions of three-center section tunnel.

Parameters	Value/Scheme
Large arch radius/mm	366
Small arch radius/mm	132
Width/mm	520
Wall height/mm	226
Length/m	16
Temperature/°C	15
Viscosity/(m^2/s)	14.4×10^{-6}
$C_{1\varepsilon}$	1.44
$C_{2\varepsilon}$	1.92
$G_{3\varepsilon}$	0.09
S_k	1.0
G_ε	0.85

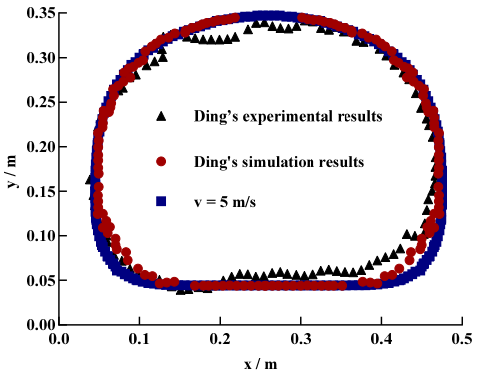


Figure 4. Results of model validation.

As shown in Figure 4, the model validation results closely align with those of Ding. While the velocity distribution shows slight variations in the lower sections of the roadway, it generally remains consistent. The discrepancy may be attributed to differences in the mesh divisions. Overall, the numerical simulation results obtained from the proposed models are deemed reliable.

3. Results and Discussion

3.1. Representative Analysis of Models with Different Scales

To investigate the relationship between the distributions of dimensionless average velocity across scaled models, the dimensionless coordinates corresponding to a velocity of 1, as shown in Figure 1, were scaled by factors of 2, 4, 8, and 10. These adjusted coordinates were then applied to the respective models to back-calculate the dimensionless velocities. The coefficient of determination (R^2) was calculated to assess the agreement between the recalculated velocities and the reference value of 1. The R^2 values for the different scale models are presented in Table 3. In addition, to evaluate the impact of temperature, air

temperatures of 15 °C, 20 °C, 25 °C, 30 °C, 35 °C, and 40 °C were set, while the wall temperature of the fixed roadway remained constant at 20 °C. The results, based on a comparison of various scaled alleyway models with simulated results, excluding the temperature field, are shown in Table 4. To assess the influence of different turbulence models, the results from the original-size standard k-epsilon model were used as a benchmark. The R^2 values for the different scale models and turbulence models were analyzed, and the results are displayed in Table 5.

Table 3. R^2 for different scale models (without considering heat transfer process).

Model Scale	R^2 of Smooth Models	R^2 of Rough Models
1	1.000	1.000
2	0.977	0.919
4	0.953	0.925
8	0.965	0.922
10	0.959	0.919

Table 4. R^2 for different scale and temperature models.

Model Scale	R^2 of Smooth Models/Rough Models				
	15 °C	20°C	25 °C	30 °C	35 °C
1	0.993/0.956	0.981/0.945	0.982/0.951	0.976/0.944	0.973/0.939
2	0.966/0.944	0.969/0.935	0.970/0.939	0.958/0.940	0.959/0.935
4	0.959/0.938	0.951/0.932	0.950/0.932	0.949/0.942	0.949/0.939
8	0.960/0.933	0.952/0.933	0.949/0.935	0.959/0.940	0.946/0.930
10	0.946/0.932	0.944/0.930	0.941/0.932	0.949/0.938	0.945/0.929

Table 5. R^2 for different turbulence models.

Model Scale	R^2 of Smooth Models/Rough Models				
	Standard $k-\varepsilon$	RNG $k-\varepsilon$	$k-\omega$	Spalart–Allmaras	LES
1	1.000/1.000	0.991/0.992	0.992/0.991	0.893/0.886	0.990/0.992
2	0.977/0.919	0.972/0.918	0.970/0.910	0.850/0.831	0.979/0.955
4	0.953/0.953	0.955/0.951	0.945/0.946	0.802/0.806	0.969/0.946
8	0.965/0.922	0.963/0.933	0.960/0.922	0.801/0.803	0.959/0.936
10	0.959/0.919	0.962/0.923	0.951/0.912	0.773/0.765	0.963/0.931

As shown in Table 3, the dimensionless velocity distribution of the scaled-up models closely aligns with that of the original model. Consequently, the analysis can be focused solely on the flow field data of the original model, ensuring its representativeness across different scales. Similarly, Table 4 indicates that the impact of the heat transfer mechanism between the air in the roadway and the roadway wall is negligible. Table 5 demonstrates that the simulation results of the LES model are more accurate than those of the Reynolds-averaged models, while the single-equation Spalart–Allmaras model exhibits lower accuracy. The results of the RNG k-epsilon and k-omega models are comparable to those of the standard k-epsilon model. However, the standard k-epsilon model offers a lower computational cost, while maintaining solution accuracy, compared to other models. Therefore, the standard k-epsilon model selected in this study is considered representative.

3.2. Dimensionless Average Velocity Distribution at Different Re

To develop a more efficient method for quantifying and analyzing average velocity in engineering applications, assessments of average velocity distribution were performed across different *Re*.

3.2.1. Dimensionless Velocity Distribution Under Laminar Regime

As mining operations extend to higher depths, the complexity of the ventilation system increases. This complexity ultimately results in short-circuit airflow, making the distribution of air volume unfeasible. Under these conditions, the airflow within the tunnel generally exhibits a laminar pattern ($1 < Re < 2100$). Figure 5 illustrates the dimensionless velocity distribution for this specific Reynolds number range, where the black line represents the dimensionless average velocity distribution ring. To analyze the distribution of average velocity rings at different speeds, the length and width of the tunnel have been non-dimensionalized accordingly. Figure 6 illustrates the dispersion of these rings across various velocities. As the velocity increases, the average velocity ring expands spatially. At the same velocity, the ring scale in the smooth model is larger than in the rough model. To further examine the velocity distribution at the center of the tunnel section, the velocity field was analyzed along the x-axis in a Cartesian coordinate system, as depicted in Figure 7. The velocity distribution at this location is highest at the center and decreases toward the periphery. As the velocity increases, the maximum dimensionless velocity decreases. Additionally, the dimensionless velocity in the smooth model is higher than that in the rough model.

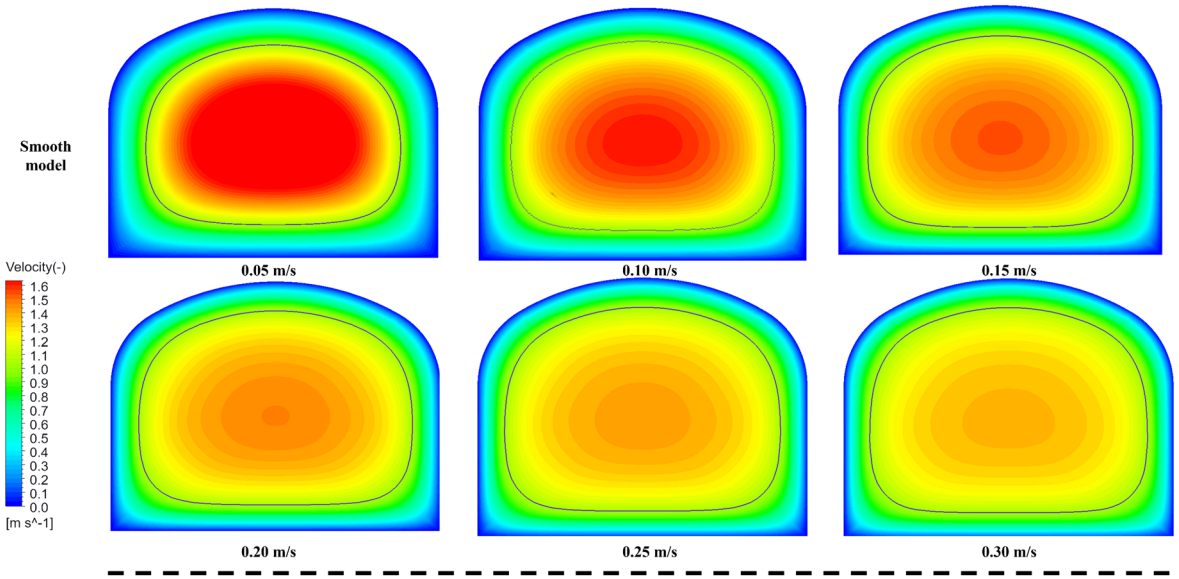


Figure 5. *Cont.*

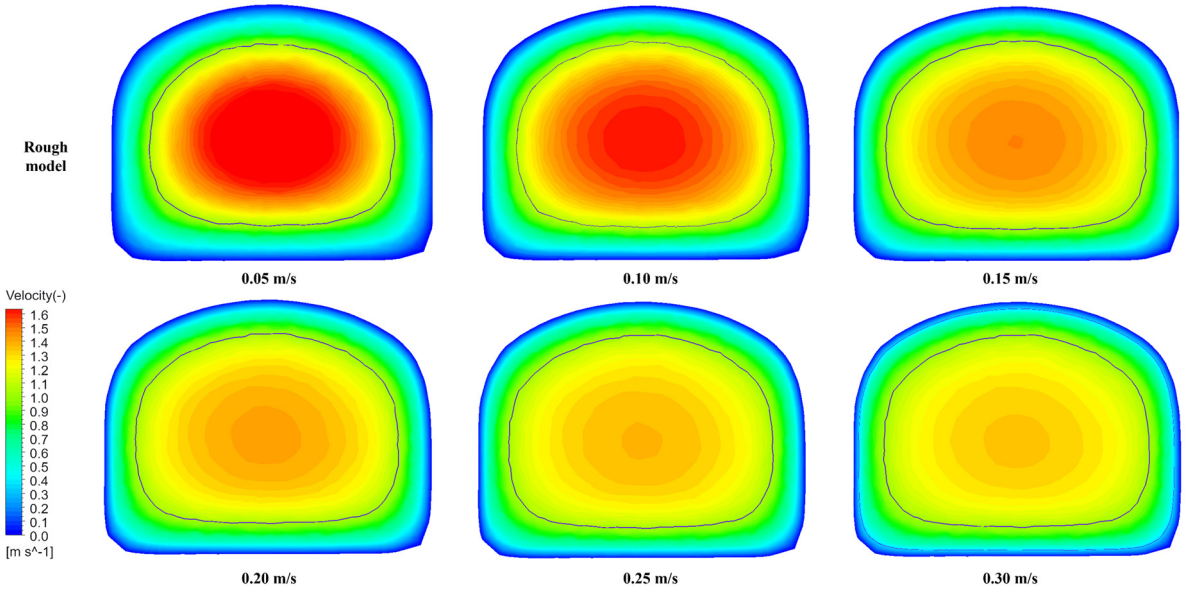


Figure 5. Dimensionless velocity distribution under laminar regime ($1 < Re < 2100$).

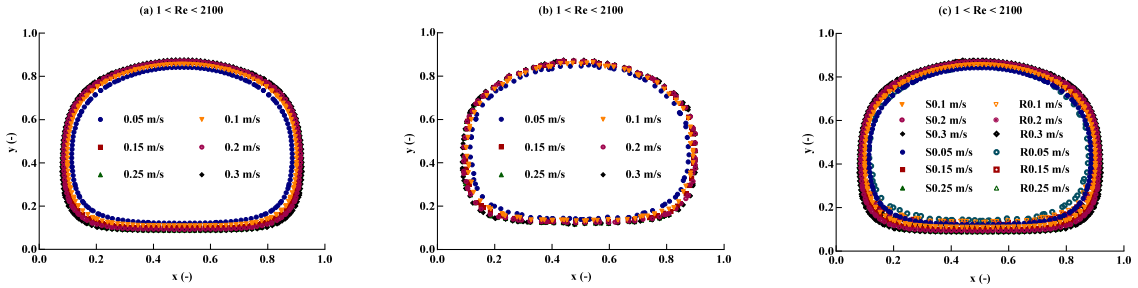


Figure 6. Dimensionless average velocity distribution under laminar regime. (**a**) Smooth model, (**b**) rough model, and (**c**) their comparisons (S: smooth model, R: rough model).

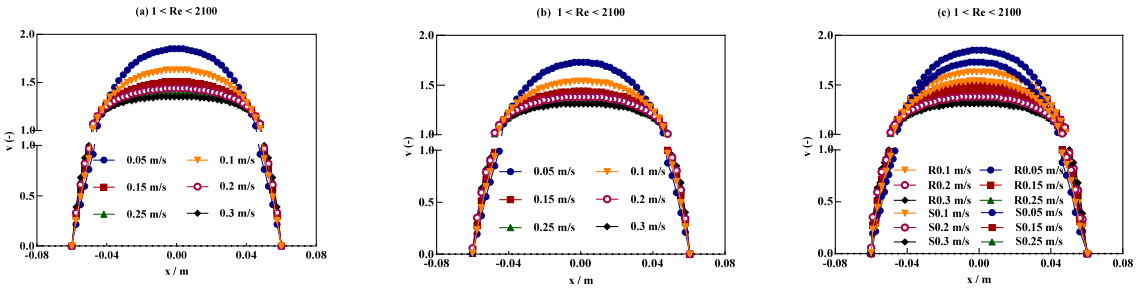


Figure 7. Dimensionless velocity distribution of central velocity field at three-centered arch cross-section. (**a**) Smooth model, (**b**) rough model, and (**c**) their comparisons (S: smooth model, R: rough model).

3.2.2. Dimensionless Velocity Distribution Under Turbulence Regime

In mine ventilation systems, the airflow is deliberately engineered to be turbulent, to enhance the safety of underground personnel and equipment. According to the simulation conditions outlined in this paper, the turbulence regime is classified as follows: for $Re > 4000$, the flow is turbulent; for $4000 < Re < 10^5$, the flow is the transition regime; and for $Re > 10^5$, the flow is the fully developed turbulence regime. The distributions of dimensionless velocity across various turbulence regimes are illustrated in Figures 8 and 11 for quantitative analysis. These figures depict the average velocity of the rings under different scenarios, as shown in Figures 9 and 12, respectively. In both the transition region and the

fully developed turbulence region, the average velocity ring distributions of the smooth and rough models are largely consistent. Similarly to the laminar condition, the dimensions of the smooth model exceed those of the rough model. When comparing the velocity distribution results at the center of the velocity field within the tunnel section parallel to the x-axis, as seen in Figures 10 and 13, it is evident that across multiple turbulence regimes, the location of the dimensionless average velocity remains largely consistent. The velocity distribution pattern is identical to that of the laminar examples. Furthermore, the integration of dimensionless velocity distribution results across different turbulence categories confirms the stable placement of the average velocity ring within the cross-sectional area of the roadway under turbulent conditions, as illustrated in Figures 14 and 15.

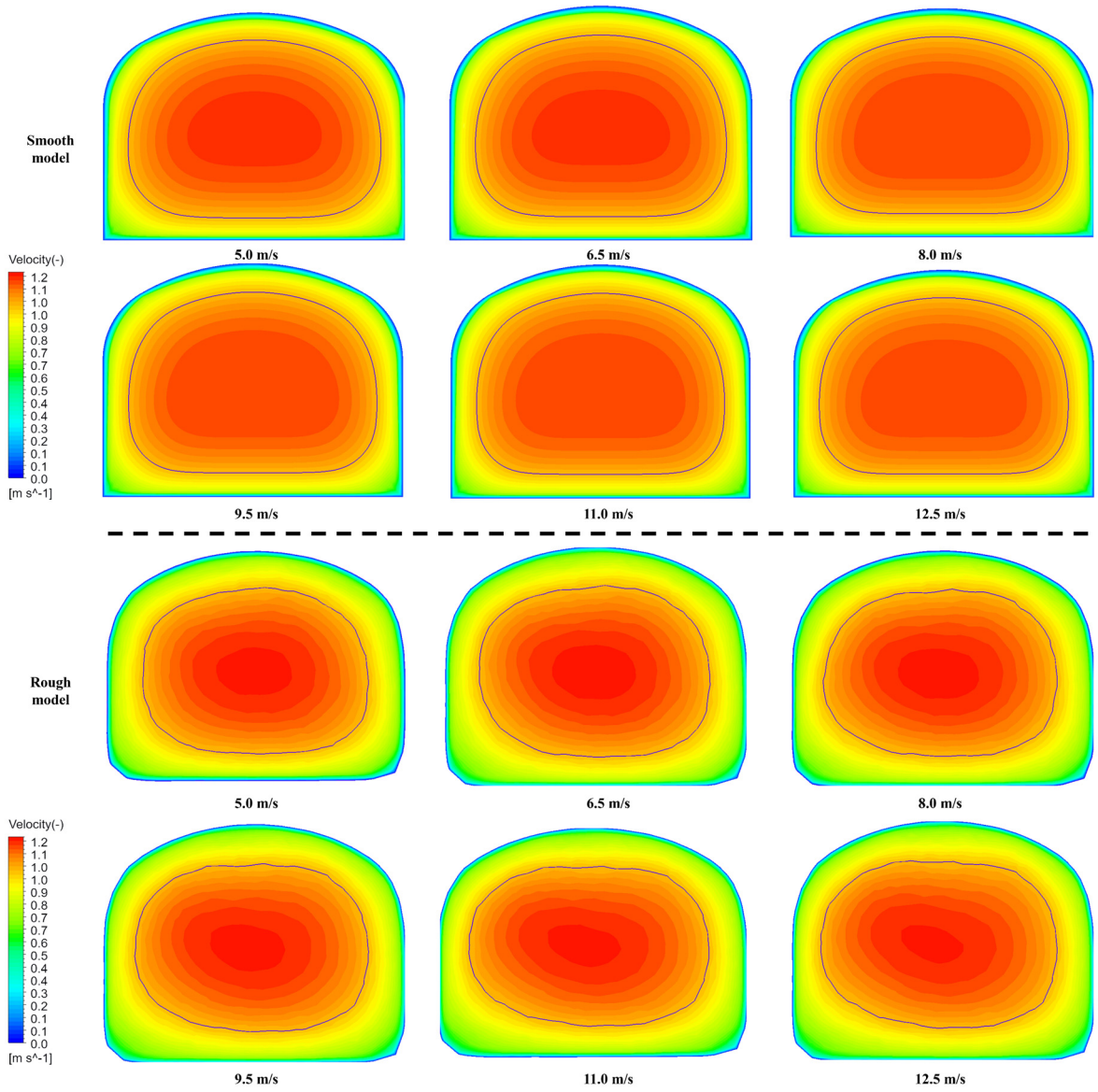


Figure 8. Dimensionless velocity distribution under transition regime.

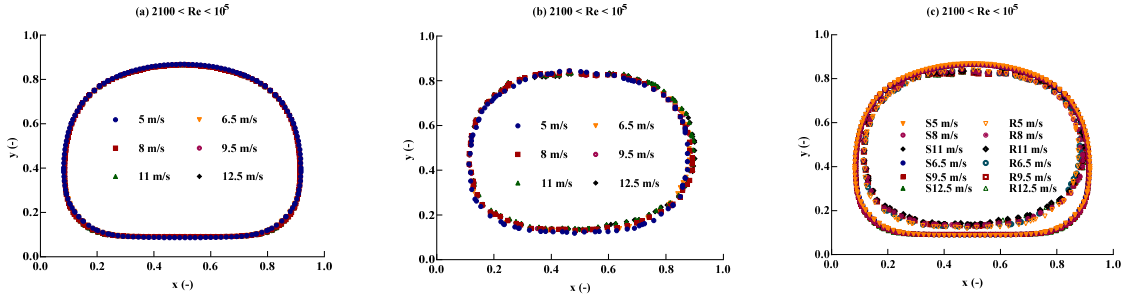


Figure 9. Dimensionless average velocity distribution under transition regime. (**a**) Smooth model, (**b**) rough model, and (**c**) their comparisons (S: smooth model, R: rough model).

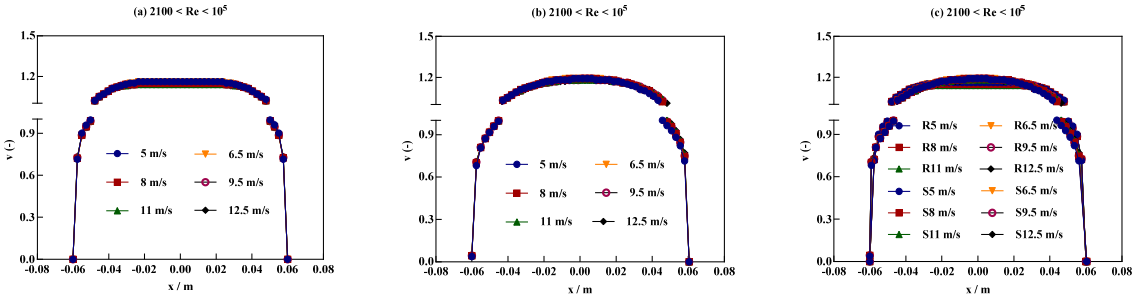


Figure 10. Dimensionless velocity distribution of central velocity field at three-centered arch cross-section under transition regime. (**a**) Smooth model, (**b**) rough model, and (**c**) their comparisons (S: smooth model, R: rough model).

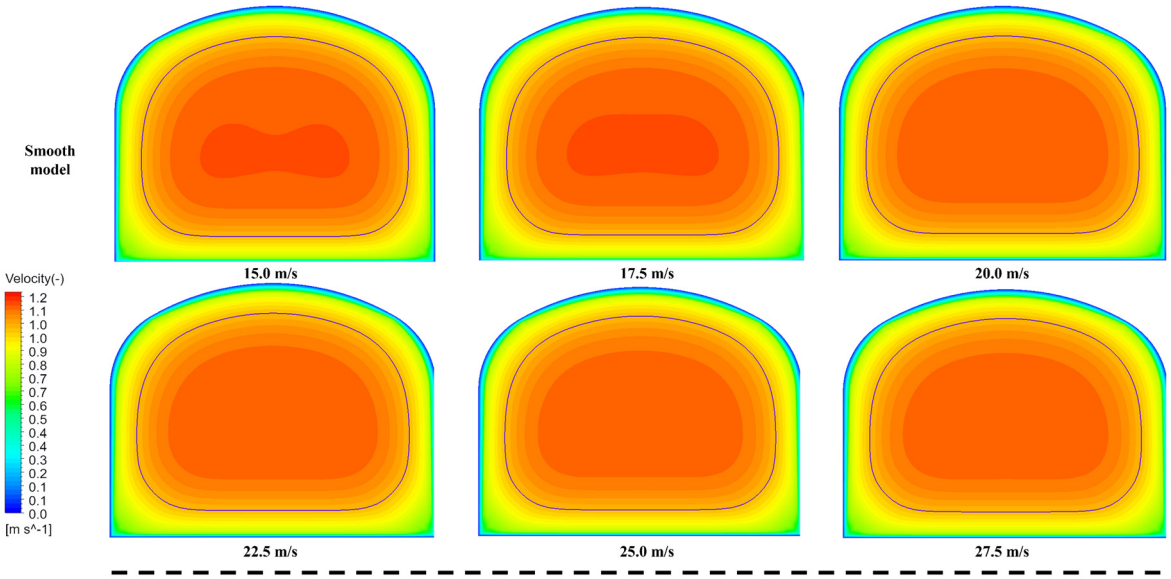


Figure 11. *Cont*.

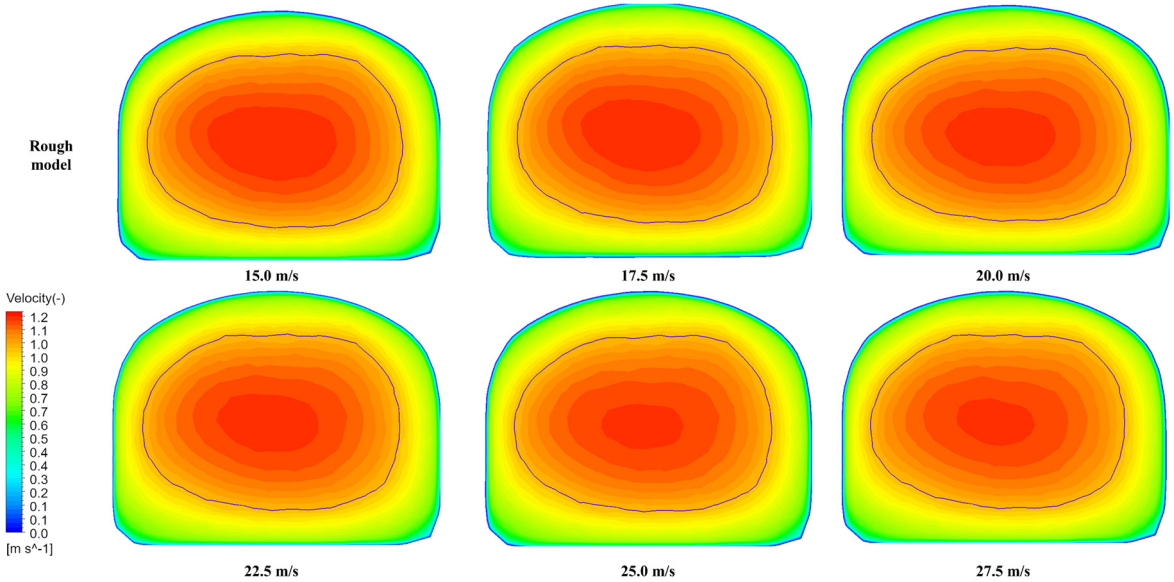


Figure 11. Dimensionless velocity distribution under fully developed turbulence regime.

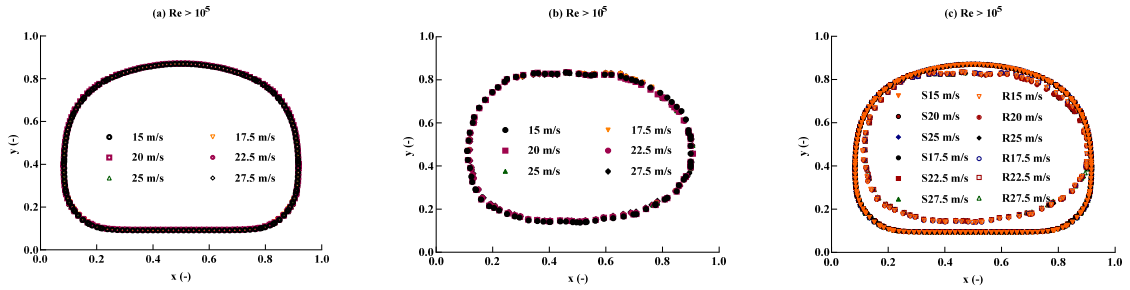


Figure 12. Dimensionless average velocity distribution under fully developed turbulence regime. (**a**) Smooth model, (**b**) rough model, and (**c**) their comparisons (S: smooth model, R: rough model).

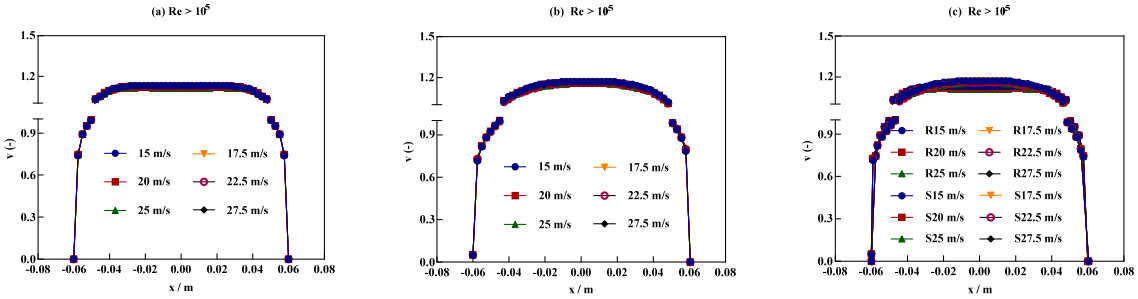


Figure 13. Dimensionless velocity distribution of central velocity field at three-centered arch cross-section under fully developed turbulence regime. (**a**) Smooth model, (**b**) rough model, and (**c**) their comparisons (S: smooth model, R: rough model).

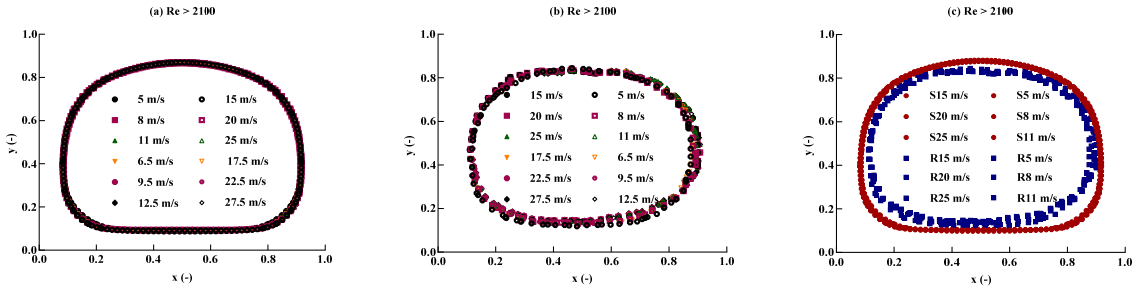


Figure 14. Dimensionless average velocity distribution under turbulence regime. (**a**) Smooth model, (**b**) rough model, and (**c**) their comparisons (S: smooth model, R: rough model).

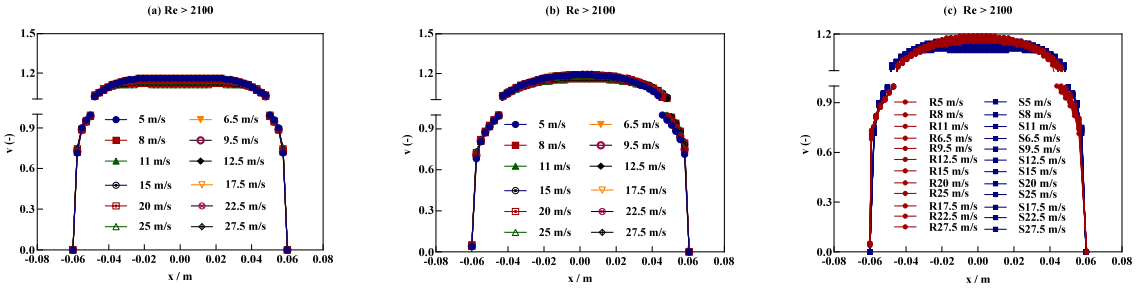


Figure 15. Dimensionless velocity distribution of central velocity field at three-centered arch cross-section under turbulence regime. (**a**) Smooth model, (**b**) rough model, and (**c**) their comparisons (S: smooth model, R: rough model).

3.3. Average Velocity Ring Position Analysis

Detection equipment for real-time monitoring of tunnel airflow is typically installed along the ceiling and sidewalls of the tunnel. This study investigates the influence of the tunnel's sidewalls and arches on the distribution of the dimensionless average velocity.

3.3.1. Determination of Core Coordinates of Average Velocity Distribution

As shown in Figures 5, 8 and 11, the maximum dimensionless velocity occurs at the center of the tunnel cross-section, corresponding to the peak of its cross-sectional velocity distribution. Accurately determining the coordinates of the center of the dimensionless average velocity distribution is essential for identifying the location of the average velocity ring.

Due to the symmetry of the tunnel structure, the center of the velocity distribution has a horizontal coordinate of $x = 0.6$ ($x\ (-) = 0.5$). The distribution of the vertical coordinates under different flow rates is shown in Table 6.

Table 6. The distribution of the dimensionless vertical coordinates of the velocity cores under different velocities.

Re Partition	Velocity (m/s)	$y\ (-)$ of Smooth Models	$y\ (-)$ of Rough Models	Average $y\ (-)$ of Smooth Models	Average $y\ (-)$ of Rough Models
Laminar regime	0.05	0.469	0.486	0.453	0.467
	0.10	0.459	0.471		
	0.15	0.454	0.476		
	0.20	0.448	0.466		
	0.25	0.448	0.456		
	0.30	0.438	0.446		

Table 6. *Cont.*

Re Partition	Velocity (m/s)	y (−) of Smooth Models	y (−) of Rough Models	Average y (−) of Smooth Models	Average y (−) of Rough Models
Transition regime	5.0	0.474	0.481	0.462	0.484
	6.5	0.464	0.486		
	8.0	0.448	0.486		
	9.5	0.469	0.486		
	11.0	0.454	0.481		
	12.5	0.464	0.486		
Fully developed turbulence regime	15.0	0.464	0.476	0.468	0.484
	17.5	0.474	0.481		
	20.0	0.469	0.481		
	22.5	0.469	0.486		
	25.0	0.470	0.491		
	27.5	0.459	0.486		

In this paper, the average y (−) is defined as the dimensionless vertical coordinate of the geometric center of the average velocity ring.

3.3.2. Effect of Tunnel Sidewalls on Dimensionless Average Velocity Distribution

Figure 16 presents a schematic representation of the dimensionless distance between the averaged velocity ring and the sidewalls, where h (−) represents the dimensionless distance at the top of the arch, and d (−) denotes the dimensionless distance at the sidewalls.

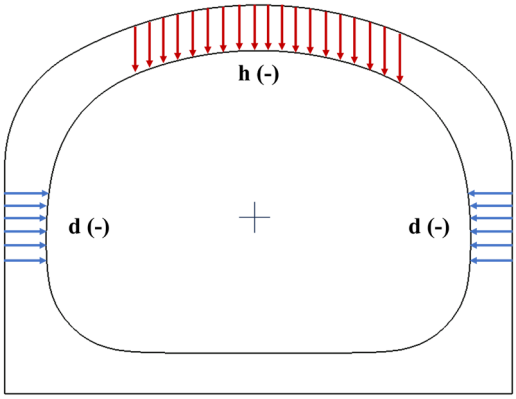


Figure 16. Schematic of dimensionless average velocity ring with dimensionless cross-section. (The blue arrow represents d (−), and the red one represents h (−)).

The objective of examining d (−) and velocity is to establish a theoretical framework for the airflow detector installation. Figure 17 displays a histogram of the d (−) distribution for different flow patterns. The red and blue dashed lines in the figures represent the average d (−) values for the smooth and rough models, respectively.

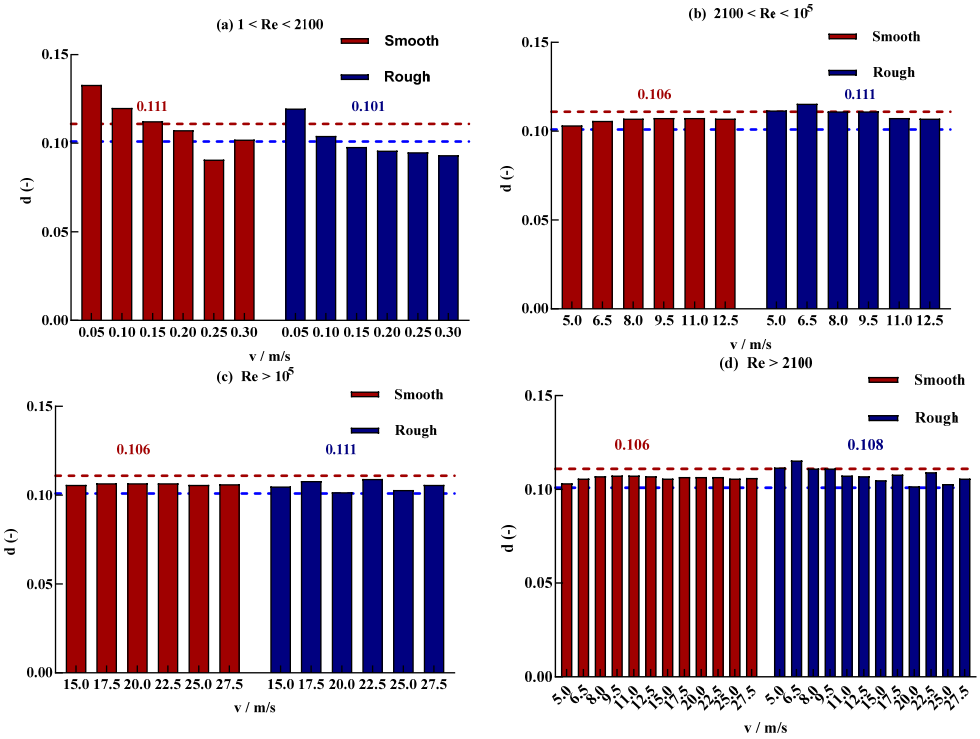


Figure 17. d $(-)$ distribution under different flow regimes. (**a**) Laminar regime, (**b**) transition regime, (**c**) fully developed turbulence regime, and (**d**) turbulence regime.

As depicted in Figure 17a, $d(-)$ and velocity exhibit a negative correlation in both the smooth and rough models under the laminar regime. The average d $(-)$ values for the smooth and rough models are 0.111 and 0.100, respectively. Figure 17b–d demonstrate no significant correlation between d $(-)$ and velocity, with d $(-)$ values remaining consistent across varying velocities. In the transition regime, the average d $(-)$ values are 0.106 and 0.111 for smooth and rough models, respectively. Similarly, the average d $(-)$ values under the fully developed turbulence regime are 0.106 and 0.111 for the smooth and the rough models, respectively. Compared with the distribution of d $(-)$ under the laminar regime, the average values of d $(-)$ are 0.106 and 0.108 for smooth and rough models under the turbulence regime. The values of d $(-)$ for the smooth model and rough model are essentially equal. Additionally, in the laminar regime, the d $(-)$ values for the smooth models are higher than those for the rough models, whereas, in the turbulence regime, the d $(-)$ values for the rough models are higher.

According to Ding [7], the distance of the sidewalls from the average velocity ring is derived as a function of the height of the wall of the roadway, as depicted in Equation (14). The dimensions of the three-center arch tunnel of Ding's models are shown in Table 7. The dimensionless distance can be obtained by dividing d by the width w. In engineering applications, smaller quantities are often neglected. The dimensionless d can be approximately expressed by Equation (15). Since $\frac{h}{w}$ is a constant value, $d'(-)$ is 0.0964, while in this study, d $(-)$ is 0.106 and 0.108 for smooth and rough models, respectively, under the turbulence regime, with the relative errors compared to this study equaling 9.40% and 10.82%, respectively.

$$d = 0.2219h - 0.0014 \tag{14}$$

$$d'(-) = 0.2219\frac{h}{w} \tag{15}$$

where d is the distance of the sidewalls from the average velocity ring, h is the height of the wall, and $d'(-)$ is the dimensionless form of d.

Table 7. Dimensions of three-center arch tunnels of Ding's models.

Large Arch Radius/mm	Small Arch Radius/mm	Width/mm	Wall Height/mm	Length/m
183	66	260	113	8
366	132	520	226	16
549	198	780	339	24
732	264	1040	452	32
915	330	1300	565	40

3.3.3. Effect of Tunnel Arches on Dimensionless Average Velocity Distribution

Compared to $d\ (-)$, the values of $h\ (-)$ are higher under the same condition. The distribution of $h\ (-)$ under different flow patterns is shown in Figure 18. As depicted in Figure 18a, the distribution of $h\ (-)$ follows a trend similar to that of $d\ (-)$, exhibiting a roughly negative correlation with velocity under the laminar regime for both the smooth and rough models. The average values of $h\ (-)$ for the smooth and rough models are both 0.135. According to Figure 18b–d, under the turbulence regime, the averaged values of $h\ (-)$ for the rough model are higher than those for the smooth model. Under both the transition and fully developed turbulence regimes, the mean values of $h\ (-)$ are identical for the smooth and rough models, respectively. Specifically, under the transition regime, the mean $h\ (-)$ values are 0.133 for the smooth model and 0.159 for the rough model. Similarly, under the fully developed turbulence regime, the mean $h\ (-)$ values are 0.129 for the smooth model and 0.166 for the rough model. Overall, in both turbulence regimes, the average $h\ (-)$ values are 0.131 for the smooth model and 0.162 for the rough model.

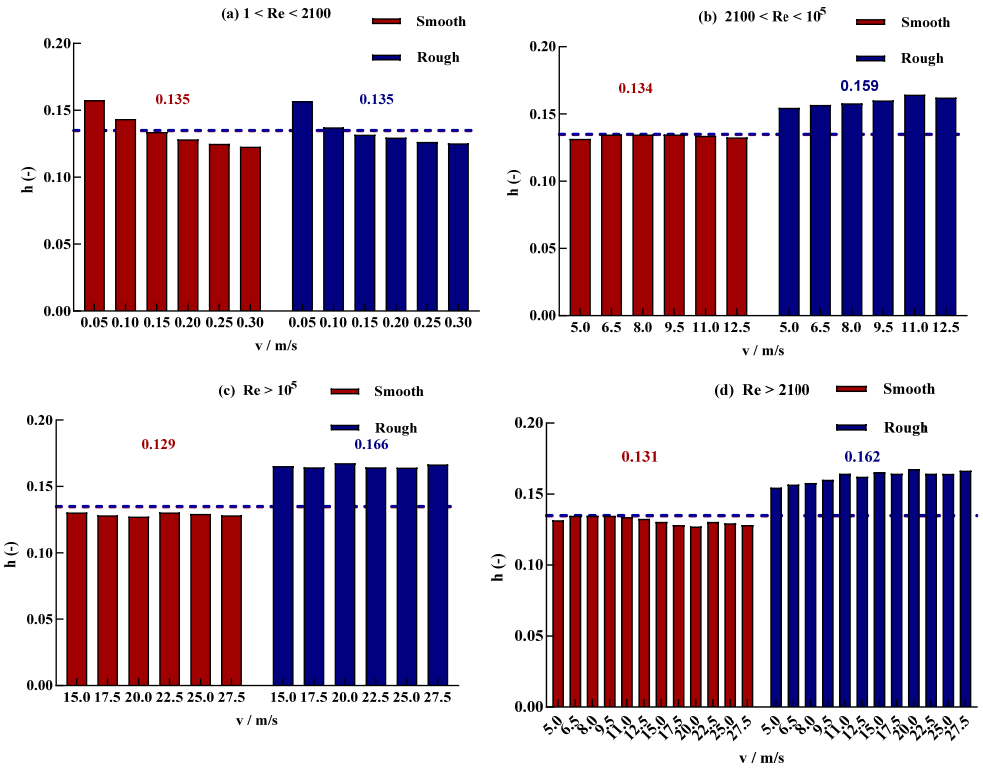


Figure 18. $h\ (-)$ distribution under different flow regimes. (**a**) Laminar regime, (**b**) transition regime, (**c**) fully developed turbulence regime, and (**d**) turbulence regime.

3.3.4. Derivation of Dimensionless Characteristic Circle Radius

In real mine ventilation tunnels, the tunnel walls are typically rough, and the airflow is often turbulent. Therefore, establishing a dimensionless average velocity ring equation

under a turbulence regime based on the rough model is of practical significance. The geometric center coordinates of the average velocity ring for the rough model under the turbulence regime are given in Table 7 as $x\ (-) = 0.5$ and $y\ (-) = 0.484$. To formulate the equation, determining the radius is essential. Using the Least Squares Method, the dimensionless radius of the average velocity ring is calculated as 0.38. Based on this, an approximate equation for the average velocity ring is derived, which has significant engineering applications.

3.4. Derivation of Velocity Distribution Equations

In the realm of physics and fluid mechanics, a boundary layer refers to a thin layer of fluid that is situated immediately adjacent to a bounding surface, which is produced by the fluid's flow alongside the surface [33]. As shown in Figures 10 and 12–14, the velocity distribution exhibits a distinct pattern under the turbulence regime. Notably, this study analyzes only half of the domain, due to its inherent symmetry.

In this study, a suitable fitting model was applied to fit the averaged velocities for the rough models under the turbulence regime, with the results shown in Table 8 and Figure 19. The linear fit of V_{max} and velocity, and the second-order polynomial fit of K_m and velocity, are shown in Figures 20 and 21.

Table 8. Results of data fitting based on fitting model.

Velocity/(m/s)	V_{max}	K_m	R^2
5.0	1.224	0.0209	0.984
6.5	1.219	0.0188	0.985
8.0	1.220	0.0182	0.986
9.5	1.218	0.0177	0.988
11.0	1.212	0.0166	0.989
12.5	1.210	0.0157	0.990
15.0	1.200	0.0143	0.992
17.5	1.195	0.0141	0.990
20.0	1.186	0.0133	0.991
22.5	1.185	0.0133	0.990
25.0	1.180	0.0125	0.992
27.5	1.179	0.0124	0.991

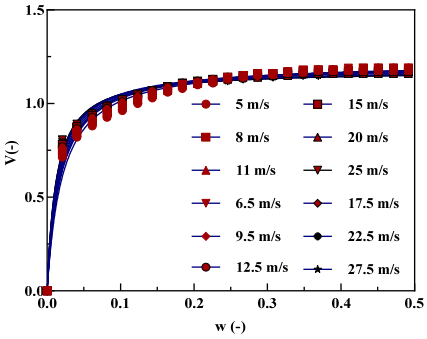


Figure 19. Results of data fitting based on fitting model.

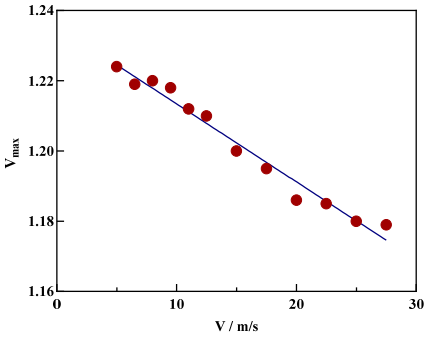


Figure 20. Linear fit of V_{max} and velocity.

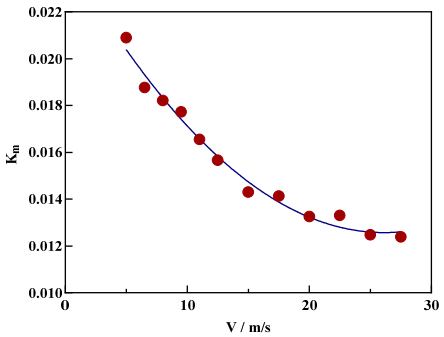


Figure 21. Second-order polynomial fit of K_m and velocity.

The resulting equations fitted are shown below:

$$V_{max} = 0.0001157V + 0.001924 \; R^2 = 0.9735 \tag{16}$$

$$K_m = 0.02453 - 0.0009152V + 1.751 \times 10^{-5}V^2 \; R^2 = 0.9852 \tag{17}$$

Therefore, under turbulence regime, the velocity distribution can be written as follows:

$$V(-) = \frac{(0.0001157V + 0.001924)w(-)}{0.02453 - 0.0009152V + 1.751 \times 10^{-5}V^2 + w(-)} \tag{18}$$

where $w(-)$ is the dimensionless distance from the sidewalls, V is the velocity, and $V(-)$ is the dimensionless velocity.

According to Equation (18), anemometers in the field cannot be strictly installed at the exact location of the average velocity distribution within the roadway cross-section. Instead, using Equation (18), the flow velocity can be measured at a single point and solved directly, or, alternatively, measurements can be taken at two or more points, with the average value providing a more representative result.

In general, the installation position of the velocity measurement device can be determined based on the direct conversion ratio.

① If the device is installed on the top or sidewall: Using the results presented in Figures 17 and 18, the corresponding dimensionless distance $d(-)$ or $h(-)$ can be converted to actual distances by multiplying them by the real tunnel width and height, respectively. The measurement location can then be determined by drawing a vertical line from the top or sidewall toward the tunnel interior.

② If the device is installed at the tunnel corners: Based on the dimensionless center coordinates (0.5, 0.484) and radius (0.38) provided in Section 3.3.4, the actual center coordinates and radius can be reverse-calculated, which, in turn, determines the specific installation location.

③ If the velocity measurement device is installed along the centerline of a cross-section parallel to the tunnel floor: At any point on this centerline, first, measure the actual speed V on the designated line. Then, use Equations (16) and (17) to calculate V_{max} and K_m, respectively. As a result, Equation (18) will have only the dependent variable $V(-)$ and the independent variable $w(-)$, thereby obtaining the analytical expression of Equation (18). By setting $V(-)$ = 1 and solving for $w(-)$, the obtained $w(-)$ can be converted into the actual distance, which determines the installation position. Additionally, if initial measurements are taken at two or more points, the final result can be obtained by averaging the computed values. The establishment of the installation location for the airflow measurement apparatus is shown in Figure 22.

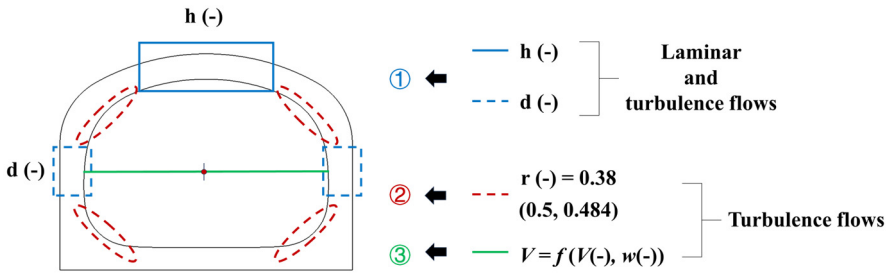


Figure 22. The establishment of the installation location for the airflow measurement apparatus.

4. Conclusions

To gain a comprehensive understanding of the airflow distribution in tunnels, and to provide a precise methodology for determining the position of the average velocity, simulations were performed on the dimensionless average velocity distribution across various flow patterns for both smooth and rough models. The key findings are summarized as follows:

- The airflow distribution exhibits a circular pattern, similar to the shape of the three-center arch section, across various flow patterns for the smooth model. In contrast, the airflow distribution of the rough model more closely resembles a perfect circle.
- The dimensionless velocity distribution at the center of the flow field, parallel to the x-axis in the tunnel cross-section, is highest in the middle and decreases on both sides. The maximum dimensionless velocity exhibits a negative correlation with velocity under the laminar regime, whereas the distribution of dimensionless velocity under the turbulence regime shows significant overlap.
- The coordinates of the center of the dimensionless average velocity rings under the turbulence regime are (0.5, 0.468) and (0.5, 0.484) for smooth model and rough model, respectively. In contrast, under the laminar regime, the coordinates are (0.5, 0.453) and (0.5, 0.467). The values of the dimensionless distance d $(-)$ are 0.111 and 0.101 for the smooth model and the rough model under the laminar regime, while under the turbulence regime, the values are 0.106 and 0.108. Similarly, the values of h $(-)$ are 0.135 and 0.135 for the smooth model and the rough model under the laminar regime, whereas under the turbulence regime, the values are 0.131 and 0.162, respectively.
- Characteristic equations based on rough models, which more accurately reflect real tunnel conditions, were developed to offer a reliable method for determining the position of the average velocity ring. The velocity distribution equation for the roadway centerline was derived using a fitting model. This model can be applied to back-calculate and determine the optimal locations for installing a mine anemometer.

Author Contributions: Methodology, Z.J. and Q.Z.; Validation, Y.Z.; Resources, T.S.; Writing—original draft, Z.J.; Writing—review & editing, Q.Z.; Supervision, Q.Z.; Funding acquisition, B.C. All authors have read and agreed to the published version of the manuscript.

Funding: This work was supported by the State Key Laboratory of Intelligent Optimized Manufacturing in Mining & Metallurgy Process (GRIMM-KZSKL-2022-11).

Data Availability Statement: The original contributions presented in this study are included in the article. Further inquiries can be directed to the corresponding author.

Conflicts of Interest: All authors disclose no relevant relationships.

References

1. Xu, G.; Jong, E.C.; Luxbacher, K.D.; McNair, H.M. Effective utilization of tracer gas in characterization of underground mine ventilation networks. *Process. Saf. Environ.* **2016**, *99*, 1–10.
2. Zhang, X.Q.; Cheng, W.M.; Zhang, Q.; Yang, X.X.; Du, W.Z. Partition airflow varying features of chaos-theory-based coalmine ventilation system and related safety forecasting and forewarning system. *Int. J. Min. Sci. Technol.* **2017**, *27*, 269–275.
3. Wang, Z.; Shao, L.; Yang, C. Fuzzy prediction of the mine's ventilation structure's tunnel air volume. *Expert. Syst. Appl.* **2023**, *231*, 120843.
4. Eggels, J.G.M.; Unger, F.; Weiss, M.H.; Westerweel, J.; Adrian, R.J.; Friedrich, R.; Nieuwstadt, F.T.M. Fully developed turbulent pipe flow: A comparison between direct numerical simulation and experiment. *J. Fluid Mech.* **1994**, *268*, 175–210.
5. Ding, C. Study on the distribution characteristics of "Characteristic Ring" in irregular cross-section ventilation roadway. In Proceedings of the 2020 6th International Conference on Advances in Energy, Environment and Chemical Engineering, Jinan, China, 19–21 June 2020; Volume 546, p. 042013.
6. Ding, C. Numerical and experimental resreach on the average velocity distribution in the trapezoid tunnels. *J. Saf. Sci. Technol.* **2016**, *12*, 28–32.
7. Ding, C.; He, X.; Nie, B. Numerical simulation of airflow distribution in mine tunnels. *Int. J. Min. Sci. Technol.* **2017**, *27*, 663–667. [CrossRef]
8. Ding, C.; Meng, Y. Simulation and experimental study on the airflow distribution in rectangular cross-section tunnels. In Proceedings of the 2020 6th International Conference on Advances in Energy, Environment and Chemical Engineering, Jinan, China, 19–21 June 2020; Volume 446, p. 052100.
9. Zhang, Q.; Luo, G.; Zou, S. Study on the distribution law of airflow velocity in rectangular and semicircular roadway sections. *Energy. Sci. Eng.* **2022**, *10*, 4150–4175.
10. Yao, Y.H. Numerical Simulation Analysis of the Influence of Entrance Wind Speed on the Wind Speed Distribution of Coal Mine Tunnel Sections. *Acad. J. Sci. Technol.* **2023**, *7*, 208. [CrossRef]
11. Parra, M.T.; Villafruela, J.M.; Castro, F.; Méndez, C. Numerical and experimental analysis of different ventilation systems in deep mines. *Bluid. Environ.* **2006**, *41*, 87–93. [CrossRef]
12. Hasheminasab, F.; Bagherpour, R.; Aminossadati, S. Numerical simulation of methane distribution in development zones of underground coal mines equipped with auxiliary ventilation. *Tunn. Undergr. Space Technol.* **2019**, *89*, 68–77.
13. Gao, K.; Liu, Z.; Li, X.; Liu, Y. Study on obtaining average velocity in a tunnel by measuring single-point air velocity. *Fresenius Environ. Bull.* **2021**, *30*, 171–180.
14. Tominaga, A.; Nezu, I. Turbulent Structure in Compound Open-Channel Flows. *J. Hydraul. Eng.* **1991**, *117*, 21–41.
15. Dahlburg, J.; Dahlburg, R.; Gardner, J.; Picone, J. Inverse cascades in two-dimensional compressible turbulence. I. Incompressible forcing at low Mach number. *Phys. Fluids A Fluid Dyn.* **1990**, *2*, 1481–1486.
16. Roller, S.; Munz, C.-D. A low Mach number scheme based on multi-scale asymptotics. *Comput. Vis. Sci.* **2000**, *3*, 85–96. [CrossRef]
17. Toutant, A. Numerical simulations of unsteady viscous incompressible flows using general pressure equation. *J. Comput. Phys.* **2018**, *374*, 822–842.
18. Cabezas Gómez, L.; Milioli, F.E. Numerical study on the influence of various physical parameters over the gas–solid two-phase flow in the 2D riser of a circulating fluidized bed. *Powder Technol.* **2003**, *132*, 216–225.
19. Nie, W.; Guo, C.; Zhang, S.; Peng, H.; Xu, C.; Ma, Q.; Yuan, M.; Zhou, W.; Guo, L.; Cheng, L. Optimization of spraying dust reduction technology of continuous miner machine and the dust environment in a tunnel, based on computational fluid dynamics (CFD) technology. *Powder Technol.* **2022**, *398*, 117044.
20. Zhai, G.; Zhang, W.; Li, Y.; Lu, X.; Hu, W. Experimental Research and Numerical Simulation of Ejector Precipitator in a Fully Mechanized Mining Face. *Arab. J. Sci. Eng.* **2020**, *45*, 9815–9833.
21. Go, M. Turbulence Models for the Numerical Prediction of Transitional Flows with RANSE. Master's Thesis, Massachusetts Institute of Technology, Cambridge, MA, USA, 2015; p. 1.

22. Talebpour, M. Numerical Investigation of Turbulent-Driven Secondary Flow. Master's Dissertation, Pennsylvania State University, University Park, PA, USA, 2016; p. 18.
23. Tabatabaei, N.; Vinuesa, R.; Örlü, R.; Schlatter, P. Techniques for turbulence tripping of boundary layers in RANS simulations. *Flow Turbul. Combust.* **2022**, *108*, 661–682.
24. Toraño, J.; Torno, S.; Menéndez, M.; Gent, M. Auxiliary ventilation in mining roadways driven with roadheaders: Validated CFD modelling of dust behaviour. *Tunn. Undergr. Space Technol.* **2011**, *26*, 201–210. [CrossRef]
25. Cengel, Y.; Cimbala, J. *Fluid Mechanics Fundamentals and Applications (Si Units)*; McGraw Hill: Boston, MA, USA, 2013; p. 322.
26. Björck, Å. Least squares methods. In *Handbook of Numerical Analysis*; Elsevier: Amsterdam, The Netherlands, 1990; Volume 1, pp. 465–652.
27. Menke, W. Review of the generalized least squares method. *Surv. Geophys.* **2015**, *36*, 1–25.
28. Flater, D. Redressing grievances with the treatment of dimensionless quantities in SI. *Measurement* **2017**, *109*, 105–110.
29. Deyhle, H.; Bippes, H. Disturbance growth in an unstable three-dimensional boundary layer and its dependence on environmental conditions. *J. Fluid Mech.* **1996**, *316*, 73–113.
30. Cornet, I.; Barrington, E.A.; Behrsing, G.U. Effect of Reynolds Number on Corrosion of Copper by Sulfuric Acid. *J. Electrochem. Soc.* **1961**, *108*, 947.
31. Abraham, J.P.; Sparrow, E.M.; Minkowycz, W.J. Internal-flow Nusselt numbers for the low-Reynolds-number end of the laminar-to-turbulent transition regime. *Int. J. Heat Mass Transf.* **2011**, *54*, 584–588.
32. Ding, C. Experimental and Numerical Study of "Key Ring" of Airflow Status in the Mine Tunnel. Ph.D. Thesis, University China University of Mining & Technology, Beijing, China, 2013; p. 52.
33. Clauser, F.H. The turbulent boundary layer. *Adv. Appl. Mech.* **1956**, *4*, 51.

Disclaimer/Publisher's Note: The statements, opinions and data contained in all publications are solely those of the individual author(s) and contributor(s) and not of MDPI and/or the editor(s). MDPI and/or the editor(s) disclaim responsibility for any injury to people or property resulting from any ideas, methods, instructions or products referred to in the content.